Chinese Chemical Letters 32 (2021) 3948–3953

Contents lists available at ScienceDirect

Chinese Chemical Letters

journal homepage: www.elsevier.com/locate/cclet

Communication

Tumor microenvironment triggered local oxygen generation and photosensitizer release from manganese dioxide mineralized albumin-ICG nanocomplex to amplify photodynamic immunotherapy efficacy

Ning Jiang[a,1], Zaigang Zhou[b,c,1], Wei Xiong[d], Jiashe Chen[b,c], Jianliang Shen[b,c,*], Rongtao Li[a,*], Ruirong Ye[a,*]

[a] Faculty of Life Science and Technology, Kunming University of Science and Technology, Kunming 650500, China
[b] State Key Laboratory of Ophthalmology, Optometry and Vision Science, School of Ophthalmology and Optometry, School of Biomedical Engineering, Wenzhou Medical University, Wenzhou 325027, China
[c] Wenzhou Institute, University of Chinese Academy of Sciences, Wenzhou 325001, China
[d] Department of Urology, Xiangya Hospital, Central South University, Changsha 410008, China

ARTICLE INFO

Article history:
Received 13 January 2021
Revised 11 June 2021
Accepted 21 June 2021
Available online 1 July 2021

Keywords:
Photodynamic therapy
Bio-mineralized method
Hypoxia
Indocyanine green
Manganese dioxide

ABSTRACT

Photodynamic therapy (PDT) has emerged as a potential clinical strategy for tumor therapy. It can generate reactive oxygen species (ROS) to cause the chemical damage of tumor cells and promote the immune killing effects of T cells on tumor cells in the presence of enough oxygen and PDT drugs. However, most solid tumors are in a state of oxygen deficiency, which seriously limit the efficacy of PDT in generation enough ROS. Besides, few safe PDT drugs with ideal pharmacokinetic behavior are available in the clinic, which severely limits the clinical transformation and application of PDT. Herein, we utilized manganese chloride to mineralize the hydrophilic indocyanine green/albumin polyplexes (ICG@BSA@MnO_2) by using bio-mineralized method to solve these problems of PDT. These ICG@BSA@MnO_2 nanoparticles could circulate in the blood for a long period other than quickly removed from body after 30 min like free ICG. When accumulated at the tumor site, ICG was responsively released in the presence of hydrogen peroxide. Apart this, the tumor hypoxia microenvironment was also reversed owing to enhanced O_2 generation by the reaction of MnO_2 with hydrogen peroxide. Benefits from the rich accumulation of ICG and ameliorated tumor hypoxia in the tumor sites, the enhanced generation of ROS could successfully promote the distribution of $CD3^+$ and $CD8^+$ T cells inside the tumors, which then lead to the amplified efficacy of PDT in both CT26 and B16F10 tumor models without causing any side effects.

In the last few decades, PDT has become one of the most effective local treatments for solid tumors [1,2]. It could generate reactive oxygen species (ROS) in the presence enough PDT drugs and sufficient oxygen, as well as initiating the antitumor immunity by promoting antigen presentation to cytotoxic T lymphocytes (CTL) to form a systemic immune effect [3–5]. Due to its merits like non-invasion and high spatiotemporal controllability, PDT is expected to become an effective tumor therapy to treat cancer in the near run [6].

Although PDT possess numerous advantages compared to other tumor therapies, its usage in clinic is still very limited [7,8]. The main cause of this status was due to the lack of safe and effective PDT molecules for clinical usage [6,8]. As we all known, a lot of PDT molecules have been discovered in the past few years, such as near-infrared photodynamic molecules, quantum dot and inorganic nano-sheets [6]. Although these molecules or nanoparticles possess ideal ROS production ability and show obvious tumor cell growth inhibition capacity, their potential hepatorenal toxicity and some unknown potential toxicity still limit their prospect of clin-

* Corresponding authors.
E-mail addresses: shenjl@wiucas.ac.cn (J. Shen), rongtaolikm@163.com (R. Li), yerr@mail2.sysu.edu.cn (R. Ye).
[1] These authors contributed equally to this work.

https://doi.org/10.1016/j.cclet.2021.06.053
1001-8417/

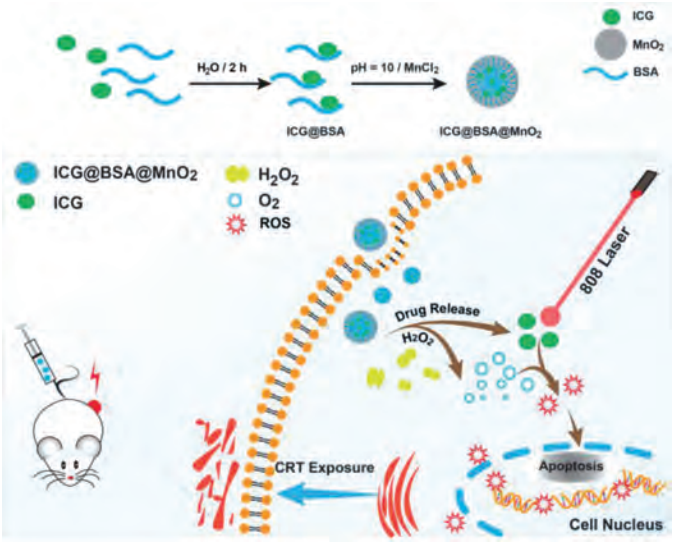

Scheme 1. Schematic illustration of the synthesis route of ICG@BSA@MnO_2 nanoparticles and the mechanism of enhanced photodynamic immunotherapy mediated by relieving tumor hypoxia and selectively release of ICG *in vivo*.

ical application [9,10]. Thus, it is of great value to better enhance the efficacy of clinical used PDT molecule, especially the only clinical usable near-infrared PDT molecule indocyanine green (ICG) [8].

Currently, ICG is a diagnostic drug used to examine liver function in clinic [11]. 97% of the free ICG could be quickly removed from the blood by the liver and excreted into feces in a short time of 30 min [12,13]. When used in PDT therapy, its efficacy is very limited owing to obviously limited tumor accumulation [14]. To solve this problem, a lot of nanomaterials are developed, including liposomes and albumin nanoparticles, among which albumin nanoparticles possess the best transformation prospect since it is approved and used in clinic [15,16]. However, ICG loaded albumin nanoparticles still possess some defects, like poor blood stability and serious drug leakage in the blood, leading to the limited ICG accumulation in tumors [17,18]. Thus, avoiding the leakage of ICG from nanoparticles in the blood to achieve better drug accumulation in tumors is still urgently needed.

Currently, manganese dioxide albumin nanoparticles (MnO_2@BSA) prepared by simple bio-mineralization method are widely used in tumor therapy and diagnosis [19,20]. MnO_2@BSA prepared by this method have many advantages, including high stability, small particle size, low cost and industrial production possibility [20]. When accumulated in the tumor, MnO_2@BSA can generate enough O_2 in the presence of H_2O_2 in tumors to enhance the efficacy of oxygen-sensitive tumor therapies, especially radiotherapy and PDT [21–23]. Besides, MnO_2@BSA could also be used to selectively deliver cationic water-soluble drug to the tumor cells [23]. But, to our best knowledge, whether it could deliver hydrophilic anion drugs to tumors are rarely proven [23–25].

In this study, by using mild bio-mineralization method, we creatively utilized MnO_2@BSA to encapsulate the hydrophilic anion drug ICG to solve the problems of PDT (Scheme 1) [26–28]. ICG@BSA@MnO_2 could circulate in the blood for a long period to avoid the quick clearance of ICG from the body. When accumulated at the tumor site, hydrogen peroxide highly expressed in tumors could selectively trigger the release of ICG. Meanwhile, the tumor hypoxia microenvironment was also reversed owing to the enhanced O_2 generation by reaction of MnO_2 with hydrogen peroxide. Due to the enhanced ICG delivery and reversed tumor hypoxia, more ROS was generated, as well as the distribution of $CD3^+$ and $CD8^+$ T cells in tumors, leading to the amplified PDT efficacy in both CT26 and B16F10 tumors.

To be specific, ICG@BSA@MnO_2 was prepared by mild bio-mineralization method. Generally, ICG and BSA were firstly hybridized in deionized water to form loose complex. Then, through the redox reaction between $MnCl_2$ and BSA, stable ICG@BSA@MnO_2 was obtained. The prepared ICG@BSA@MnO_2 showed highly homogeneous spherical structure of 60.5 ± 4.3 nm with zeta potential of -38.5 ± 2.7 mV (Figs. 1A and B; Fig. S1 in Supporting information). By using elemental mapping analysis, it was confirmed that amounts of manganese and oxygen element was located in the ICG@BSA@MnO_2, meaning that MnO_2 did form a nanosystem with ICG@BSA complex (Fig. 1A). It was also further revealed that ICG was encapsulated in ICG@BSA@MnO_2 nanoparticles by NR-VIS analyse (Fig. 1C). Following this, the stability of ICG@BSA@MnO_2 was researched. Results indicated that the particle size of ICG@BSA@MnO_2 did not obviously change in the PBS buffer at pH 7.4 or 6.4 and for 10% FBS at per-set time (Fig. S2 in Supporting information). All these results revealed that ICG@BSA@MnO_2 was well prepared with highly homogeneous spherical structure and well stability.

To predict the ability of ICG@BSA@MnO_2 to release ICG and generate O_2 at the hydrogen peroxide highly expression microenvironment, the release behavior of ICG@BSA@MnO_2 at H_2O_2 *in vitro* was evaluated. Results showed that ICG would be quickly released from ICG@BSA complex, while few ICG was released from ICG@BSA@MnO_2 in the same condition (Fig. 1D). Besides, the ICG release from ICG@BSA@MnO_2 at different time with the addition of 100 μmol/L H_2O_2 was obviously enhanced, meaning that ICG@BSA@MnO_2 could be degraded by H_2O_2 to trigger the release of ICG (Figs. 1D and E). Meanwhile, it was also revealed that abundant O_2 was also generated with the reaction of H_2O_2 and ICG@BSA@MnO_2 (Fig. S3 in Supporting information). With the obviously enhanced generation of O_2 and released ICG, more ROS was generated after laser radiation, which may then cause obvious damage to tumor cells (Fig. 1F). All these results above indicated that ICG@BSA@MnO_2 possess high O_2 and ROS generation ability *in vitro* when triggered by the moderate amount of H_2O_2.

As indicated above, ICG@BSA@MnO_2 possessed high O_2 and ROS generation ability *in vitro,* we speculated that ICG@BSA@MnO_2 may enhance the efficacy of PDT *in vitro*. To prove this, the effects of ICG@BSA@MnO_2 on the tumor cell uptake was evaluated. As shown in Fig. 2A, the red fluorescence signal of ICG in CT26 tumor cells from free ICG or ICG@BSA@MnO_2 was almost all located in the cell cytoplasm after incubation for 2 h or 6 h. Besides, no obvious fluorescence signal difference was found between free ICG or ICG@BSA@MnO_2 treated cells (Fig. S4 in Supporting information), meaning that ICG@BSA@MnO_2 had no effect on the cell uptake of ICG. Then, ROS generation in CT26 cells after laser radiation were measured with DCFH-DA under hypoxia (3% O_2) and normoxia (21% O_2). As indicated, a stronger green fluorescence of ROS in CT26 cells were observed after treatment with ICG@BSA@MnO_2 together with laser radiation compared with ICG groups (Fig. 2B; Figs. S5 and S6 in Supporting information). Meanwhile, enhanced cell membrane exposure of calprotectin (CRT) was also detected in ICG@BSA@MnO_2 treated CT26 tumor cells together with laser radiation (Fig. 2B; Fig. S7 in Supporting information). All results mean that ICG@BSA@MnO_2 could enhance ROS generation and CRT exposure in CT26 cancer cells *in vitro*.

Following this, the cell viability assay was conducted by using CCK-8. As shown in Figs. 2C and D, ICG@BSA@MnO_2 and ICG without laser radiation showed no obvious toxicity to CT26 cells, suggesting that ICG@BSA@MnO_2 possess good biocompatibility. When

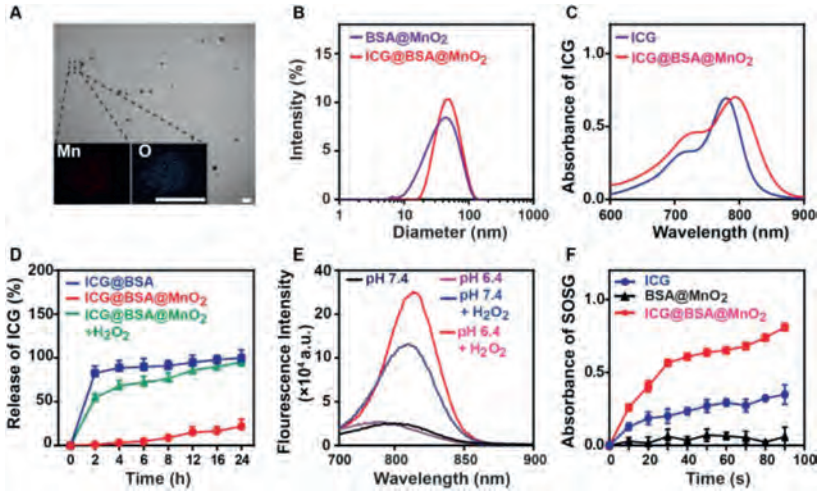

Fig. 1. Characterization of the ICG@BSA@MnO_2. (A) Representative images of TEM and energy-spectrum element scanning of the prepared ICG@BSA@MnO_2, scale bar = 100 nm. (B) Hydrodynamic diameters of BSA@MnO_2 and ICG@BSA@MnO_2. (C) UV-vis spectra of free ICG and ICG@BSA@MnO_2 in deionized water. (D) The stability of ICG@BSA and ICG@BSA@MnO_2 detected by DLS in pH 7.4 or 6.4 PBS buffer at per-set time. (E) Fluorescence spectra of ICG@BSA@MnO_2 in different PBS buffers including pH 7.4, 6.4, 7.4 plus 100 μmol/L H_2O_2 and pH 6.4 plus 100 μmol/L H_2O_2. (F) The ability of free ICG, BSA@MnO_2 or ICG@BSA@MnO_2 to generate ROS in deionized water with 100 μmol/L H_2O_2. Data were shown as mean ± SD, $n = 3$. $^{**}P < 0.01$.

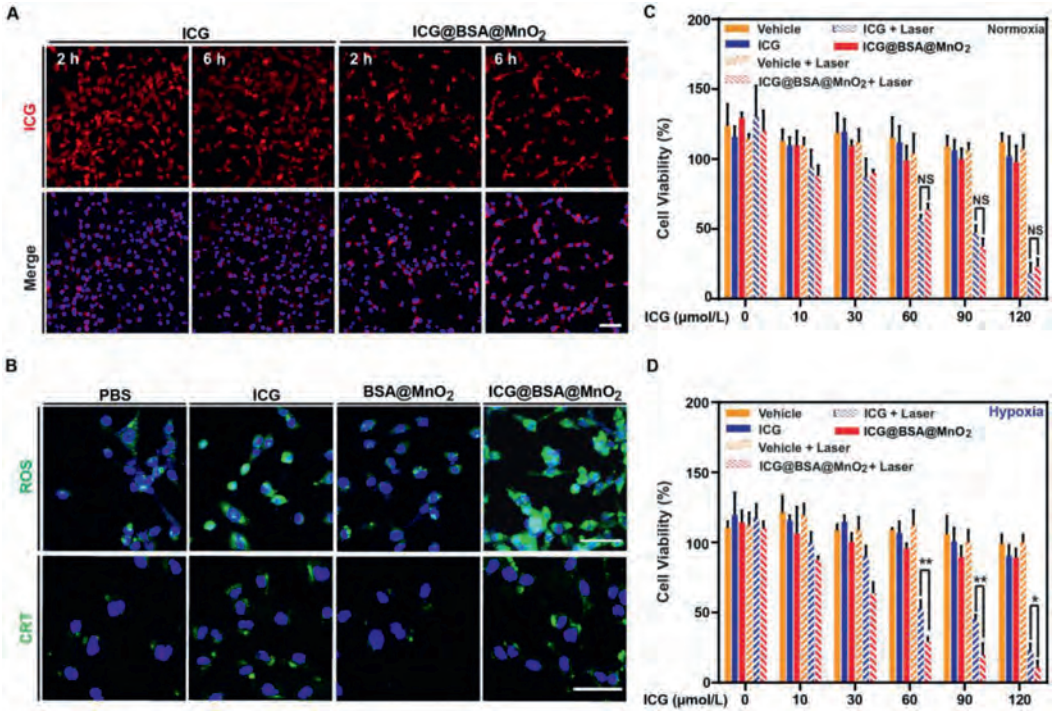

Fig. 2. ICG@BSA@MnO_2 generated more ROS and induced obvious tumor cell cytotoxicity *in vitro*. (A) Representative fluorescence images of ICG in CT26 tumor cells at 2 h and 6 h after free ICG or ICG@BSA@MnO_2 treatment, scale bar = 50 μm. (B) Representative fluorescence images of the generation of ROS and cell membrane loaction of CRT in CT26 tumor cells in hypoxia (3% O_2), scale bar = 50 μm. (C, D) Cell viability of CT26 cells detected by CCK-8 assay after indicated different treatments under normoxia (21% O_2) and hypoxia (3% O_2). Data were shown as mean ± SD, $n = 3$. $^{*}P < 0.05$, $^{**}P < 0.01$, $^{***}P < 0.001$ and NS, no significant difference.

ICG@BSA@MnO_2 or free ICG was co-treated with laser irradiation in hypoxia (3% O_2), the cell viability of ICG@BSA@MnO_2 was dramatically decreased compared with free ICG treated tumor cells (Fig. 2D). This indicated that ICG@BSA@MnO_2 mediated PDT exhibited obvious cell growth inhibition ability. Meanwhile, when ICG@BSA@MnO_2 or free ICG was co-treated with laser irradiation in normoxia (21% O_2), the difference of the ability in inhibiting the cell growth between free ICG and ICG@BSA@MnO_2 co-treated with laser irradiation disappeared (Fig. 2C), meaning that enhanced oxygen production by ICG@BSA@MnO_2 increased the cell cytotoxicity ICG@BSA@MnO_2 mediated PDT. All in all, these results above showed that ICG@BSA@MnO_2 exhibited high PDT efficacy *in vitro*.

To track the pharmacokinetics of ICG@BSA@MnO_2 *in vivo*, the blood metabolic behavior of ICG@BSA@MnO_2 was firstly evaluated. As shown in Fig. S8 (Supporting information), free ICG was quickly removed from the mice at a short period of about 30 min. But for ICG@BSA@MnO_2 treated mice, the blood residence time of ICG@BSA@MnO_2 was significantly increased. At 24 h and 48 h, the mice were sacrificed to collect the major organs and tumors. Re-

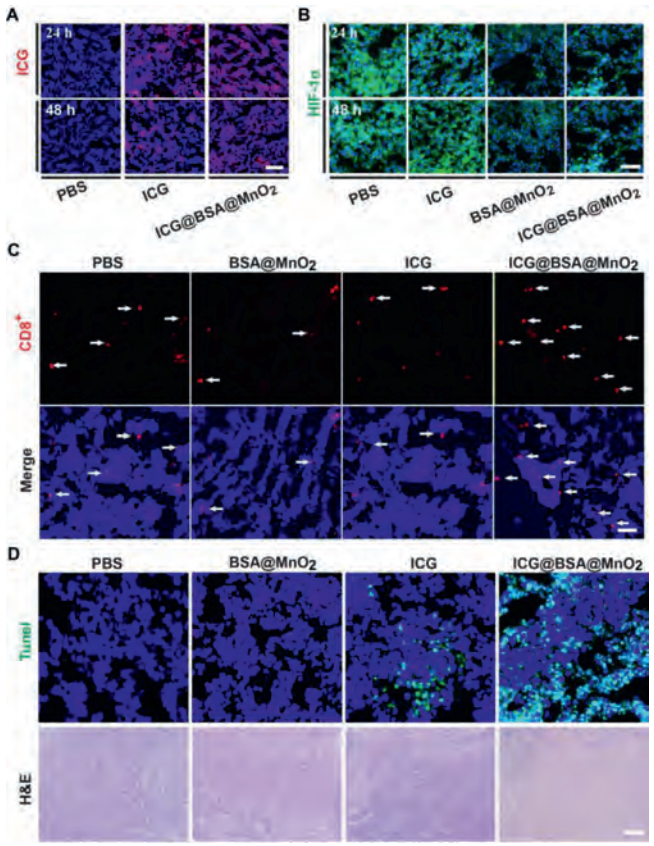

Fig. 3. ICG@BSA@MnO_2 reversed tumor hypoxia and obviously increased the infiltration of T cells and induced apoptosis in CT26 tumors. (A) Representative fluorescence images of ICG in CT26 tumors at 24 h or 48 h after intravenous injection of free ICG or ICG@BSA@MnO_2 nanoparticles, scale bar = 100 μm. (B) Representative immunofluorescence images of HIF-1α in CT26 tumor slices at 24 h and 48 h after intravenous injection of free ICG or ICG@BSA@MnO_2, scale bar = 100 μm. (C) Representative immunofluorescence images of $CD8^+$ T cells (red) in the tumor tiusses at 24 h after indicated treatments. White arrows denoted the location of $CD8^+$ T cells in the tumor tiusses, scale bar = 100 μm. (D) Representative immunofluorescence images of $Tunel^+$ CT26 tumor cells (green) at 24 h after different treatments with laser radiation, scale bar = 100 μm. H&E staining of tumor sections after different treatments in the presence of laser radiation, scale bar = 200 μm. For interpretation of the references to color in this figure legend, the reader is referred to the web version of this article.

sults indicated that more ICG was accumulated in the heart, liver, spleen, lung, kidney and tumors of ICG@BSA@MnO_2 treated mice, while almost no ICG was detected in these tissues in free ICG treated mice (Figs. S9 and S10 in Supporting information). Thus, ICG could better accumulate at the tumor site when encapsulated in ICG@BSA@MnO_2 nanoparticles (Fig. 3A; Fig. S11 in Supporting information).

As all known, MnO_2 could generate amounts of O_2 by reaction with H_2O_2 and about 100-1000 μmol/L H_2O_2 located in different types of tumors [29]. Thus, ICG@BSA@MnO_2 may also possess the ability to reverse tumor hypoxia *in vivo* in CT26 tumors. To prove this, HIF-1α and Pimonidazole, two indirect tumor hypoxia indicators, were used. As indicated, both BSA@MnO_2 and ICG@BSA@MnO_2 downregulated HIF-1α expression in CT26 tumors *in vivo*, while ICG itself did not possess this ability, meaning that MnO_2 in ICG@BSA@MnO_2 mediated the reversed tumor hypoxia microenvironment other than ICG (Fig. 3B; Fig. S12 in Supporting information). Moreover, a similar phenomenon that ICG@BSA@MnO_2 mediated the reversed tumor hypoxia was also obtained by using another hypoxia indicator Pimonidazole (Figs. S13 and S14 in Supporting information). Thus, ICG@BSA@MnO_2 could obviously reverse tumor hypoxia *in vivo*.

Very recently, it was proved that PDT could relieve T cell exhaustion by inducing immunogenic death, such as CRT [30,31]. As proved above, ICG@BSA@MnO_2 mediated PDT obviously induced CRT exposure in cell membrane (Fig. 2B). Thus, we speculated that ICG@BSA@MnO_2 mediated PDT could also relieve T cell exhaustion *in vivo*. Results indicated that the infiltration and distribution of $CD3^+$ and $CD8^+$ T cells were significantly increased in CT26 tumors treated by ICG@BSA@MnO_2 with laser radiation compared (Fig. 3C; Fig. S15 in Supporting information). Subsequently, TUNEL and H&E staining were used to evaluate anti-tumor effects of ICG@BSA@MnO_2 with laser radiation. Results showed that more CT26 tumor cells apoptosis was induced by ICG@BSA@MnO_2 mediated PDT than other groups including cells treated by free ICG and laser radiation (Fig. 3D; Fig. S16 in Supporting information). All in all, ICG@BSA@MnO_2 mediated PDT could most effectively induce the tumor cell death.

Inspired by the above results, we next evaluated the efficacy of ICG@BSA@MnO_2 mediated PDT in inhibiting CT26 tumor growth *in vivo* (Fig. 4A). All these procedures strictly complied with the ethical and legal requirements under the Administration Committee of Experimental Animals in Zhejiang Province and were approved by Ethics Committee of Wenzhou Medical University. As shown in Fig. 4B, ICG@BSA@MnO_2 + laser treatment showed the most significant tumor growth inhibition ability, while only little such effect existed in ICG + laser treated mice. The difference of efficacy between ICG@BSA@MnO_2 + laser group and ICG + laser group in inhibiting tumor growth was at least partly caused by the phenomenon ICG@BSA@MnO_2 + laser treated mice showed effectively reversed tumor hypoxia and increased ICG accumulation in tumors compared with free ICG (Figs. 3A and B). At Day 14, all mice were sacrificed to collect the tumors. Results also showed that the average tumor weight of ICG@BSA@MnO_2 + laser group was only about 25% of the tumors of PBS treated mice (Fig. 4C). Meanwhile, although the average tumor weight of ICG + laser group was slightly decreased compared with that of mice PBS treated mice, no obvious difference was found (Fig. 4C). More importantly, no significant body weight changes were observed after ICG@BSA@MnO_2 administration (Fig. S17 in Supporting information), indicating that ICG@BSA@MnO_2 possessed good biocompatibility *in vivo*.

Following this, the general validity of ICG@BSA@MnO_2 mediated PDT in inhibiting tumor growth was also researched in B16F10 tumors (Fig. 4D). The average tumor weight of ICG@BSA@MnO_2 + laser group was only about 20% of the tumors of PBS treated mice (Fig. 4E). Meanwhile, no significant body weight changes were observed after ICG@BSA@MnO_2 administration in B16F10 tumors (Fig. S17 in Supporting information). Thus, ICG@BSA@MnO_2 mediated PDT effectively inhibited tumor growth *in vivo* in different tumors.

To predict the clinical application potential of ICG@BSA@MnO_2, the biosafety of ICG@BSA@MnO_2 was researched. Results showed that the therapeutic dose of ICG@BSA@MnO_2 and BSA@MnO_2 did not cause any red blood cell hemolysis (Fig. S18 in Supporting information). Besides, ICG@BSA@MnO_2 had no effect on the renal function and liver function compared with PBS group in Balb/c mice (Figs. S19 and S20 in Supporting information). Meanwhile, BSA@MnO_2 also not inflected the renal function and liver function (Figs. S19 and S20). Moreover, Balb/c mice treated with ICG@BSA@MnO_2 and BSA@MnO_2 showed no obvious histopathological damage in the major organs compared to the PBS treated mice (Fig. S21 in Supporting information). All these results above proved that ICG@BSA@MnO_2 possessed ideal biological safety.

In conclusion, ICG@BSA@MnO_2 nanoparticles were prepared by using bio-mineralized method. By using this method, the ICG@BSA@MnO_2 nanoparticles could circulate in the blood for a

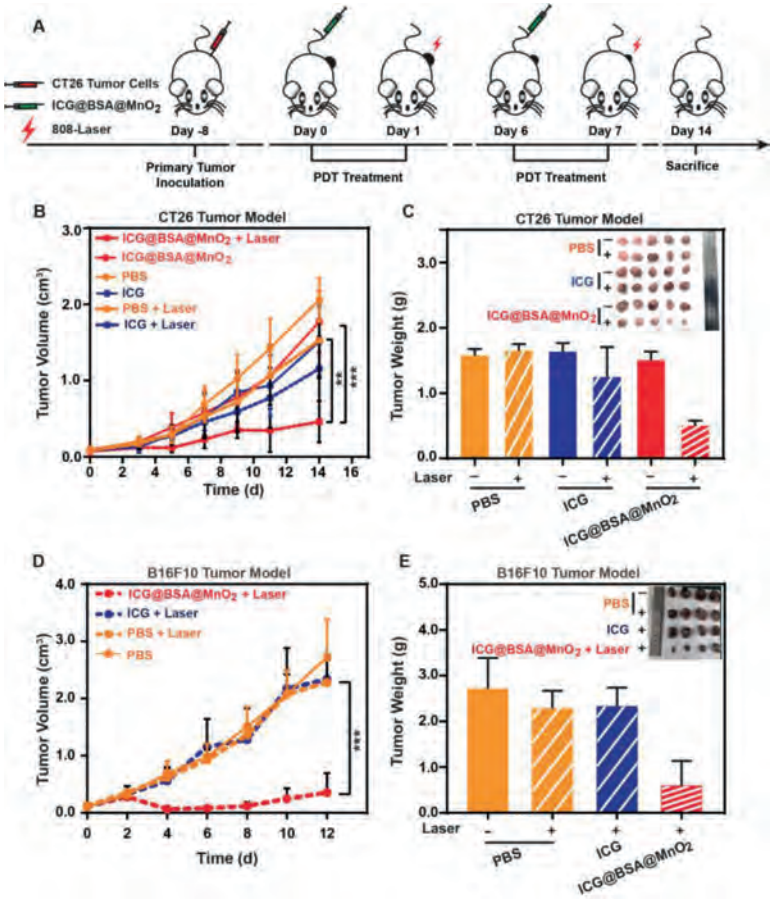

Fig. 4. Antitumor effects of ICG@BSA@MnO_2 mediated PDT in CT26 tumors. (A) Schematic illustration of tumor model establishment and the therapeutic process. (B) CT26 tumor growth curves of mice in each group: PBS; PBS + Laser; ICG; ICG + Laser; ICG@BSA@MnO_2 and ICG@BSA@MnO_2 + Laser. (C) Tumor weight and photograph of collected CT26 tumors from different groups at Day 14 after various treatments. (D) B16F10 tumor growth curves of mice in each group: PBS; PBS + Laser; ICG + Laser; and ICG@BSA@MnO_2 + Laser. (E) Tumor weight and photograph of collected B16F10 tumors from different groups at Day 14 after various treatments. Data were shown as mean ± SD, $n = 5$. $^{**}P < 0.01$, $^{***}P < 0.001$.

long period other than quickly removed in a short period of 30 min like the free ICG, leading to enhanced ICG accumulation in the tumor. In the presence of high hydrogen peroxide in tumor surroundings, ICG was selectively released. Besides, the tumor hypoxia microenvironment was also specifically reversed owing to enhanced O_2 generation. Due to the enhanced ICG delivery and reversed tumor hypoxia, more ROS was generated, as well as the distribution of $CD3^+$ and $CD8^+$ T cells in tumors, which then lead to the amplified efficacy of PDT in different tumors. Considering the fact that albumin and ICG were both widely used in clinic, ICG@BSA@MnO_2 has great potential to become a highly effective cancer treatment modality.

Declaration of competing interest

The authors declare that they have no known competing financial interests or personal relationships that could have appeared to influence the work reported in this paper.

Acknowledgments

This work was supported by the National Natural Science Foundation of China (Nos. 22007042, 31800833, 21977081, 81874094, 81974397 and 82003697), Zhejiang Provincial Natural Science of Foundation of China (No. LZ19H180001).

Supplementary materials

Supplementary material associated with this article can be found, in the online version, at doi:10.1016/j.cclet.2021.06.053.

References

[1] C. Liu, L. Zhou, F. Wei, et al., ACS Appl. Mater. Interfaces 11 (2019) 8797–8806.
[2] X. Li, S. Lee, J. Yoon, Chem. Soc. Rev. 47 (2018) 1174–1188.
[3] J. Cheng, H. Zhao, L. Yao, et al., ACS Appl. Mater. Interfaces 11 (2019) 29498–29511.
[4] G. Yang, L. Xu, Y. Chao, et al., Nat. Commun. 8 (2017) 902.
[5] W. Fan, P. Huang, X. Chen, Chem. Soc. Rev. 45 (2016) 6488–6519.
[6] U. Chilakamarthi, L. Giribabu, Chem. Rec. 17 (2017) 775–802.
[7] B.M. Luby, C.D. Walsh, G. Zheng, Angew. Chem. Int. Ed. 58 (2019) 2558–2569.
[8] X. Li, J.F. Lovell, J. Yoon, Nat. Rev. Clin. Oncol. 17 (2020) 657–674.
[9] A. Oniszczuk, K.A. Wojtunik-Kulesza, T. Oniszczuk, K. Kasprzak, Biomed. Pharmacother. 83 (2016) 912–929.
[10] S.H. Ibbotson, Photodermatol. Photoimmunol. Photomed. 27 (2011) 116–130.
[11] H. Wang, X. Li, B.W. Tse, et al., Theranostics 8 (2018) 1227–1242.
[12] X. Jiang, B. Du, J. Zheng, Nat. Nanotechnol. 14 (2019) 874–882.
[13] H. Yu, M. Ji, Mol. Imaging Biol. 23 (2021) 160–172.
[14] H. Hu, J. Chen, H. Yang, et al., Nanoscale 11 (2019) 6384–6393.
[15] H.J. Yoon, H.S. Lee, J.Y. Lim, J.H. Park, ACS Appl. Mater. Interfaces 9 (2017) 5683–5691.
[16] F. An, Z. Yang, M. Zheng, et al., J. Nanobiotechnol. 18 (2020) 49.
[17] A. Sahu, J.H. Lee, H.G. Lee, et al., J. Control. Release 236 (2016) 90–99.
[18] D. Sun, Y. Huang, X. Zhang, et al., J. Mater. Chem. B 6 (2018) 6969–6976.
[19] Y.Z. Wang, Y.J. Song, G.X. Zhu, et al., Chin. Chem. Lett. 29 (2018) 1685–1688.
[20] W.W. Zhu, Z.L. Dong, T.T. Fu, et al., Adv. Funct. Mater. 26 (2016) 5490–5498.
[21] Q. Chen, L.Z. Feng, J.J. Liu, et al., Adv. Mater. 28 (2016) 7129–7136.
[22] L. Meng, Y. Cheng, S. Gan, et al., Mol. Pharm. 15 (2018) 447–457.

[23] L. Meng, Y. Cheng, X. Tong, et al., ACS Nano 12 (2018) 8308–8322.
[24] J. Wen, K. Yang, S. Sun, Chem. Commun. 56 (2020) 7065–7079.
[25] X. Wang, K. Su, L. Tan, et al., ACS Appl. Mater. Interfaces 11 (2019) 15014–15027.
[26] J. Chen, Q. Chen, C. Liang, et al., Nanoscale 9 (2017) 14826–14835.
[27] J. Ge, R. Cai, X. Chen, et al., Talanta 195 (2019) 40–45.
[28] X. Yi, L. Chen, X.Y. Zhong, et al., Nano Res. 9 (2016) 3267–3278.
[29] L. Zhou, Y. Wu, X. Meng, et al., Small 14 (2018) e1801008.
[30] Z. Chen, L. Liu, R. Liang, et al., ACS Nano 12 (2018) 8633–8645.
[31] H. He, L. Liu, R. Liang, et al., Acta Biomater. 104 (2020) 188–197.